· Article · Advances in Polar Science
doi: 10.12429/j.advps.2024.0023 December 2024 Vol. 35 No. 4: 421-437

Characteristics of Antarctic aerosol composition during the Australian fires of 2019–2020

CHEN Afeng[1,2], WANG Longquan[1], LIU Hongwei[1], YUE Fange[1] & XIE Zhouqing[1,3*]

[1] Institute of Polar Environment & Anhui Key Laboratory of Polar Environment and Global Change, Department of Environmental Science and Engineering, University of Science and Technology of China, Hefei 230026, China;
[2] Engineering and Technological Research Centre of National Disaster Relief Equipment, Army Logistics Academy, Chongqing 401331, China;
[3] State Key Laboratory of Fire Science, University of Science and Technology of China, Hefei 230026, China

Received 2 August 2024; accepted 18 November 2024; published online 30 December 2024

Abstract During the 36th Chinese National Antarctic Research Expedition, aerosol samples were gathered from the Ross Sea in Antarctic to assess the climatic impact of the Australian fires that occurred in 2019–2020. The chemical compositions, including levoglucosan (Lev) and its isomers, galactosan (Gan) and mannosan (Man), were analyzed. Principal component analysis helped identify the potential sources of these chemical components. By combining backward trajectories with the ratios of C_{Lev}/C_{Man} and C_{Man}/C_{Gan}, it was further inferred that Australia might be the potential source region for biomass burning. The radiative forcing resulting from biomass burning was evaluated using the Santa Barbara DISORT Atmospheric Radiative Transfer (SBDART) model, which revealed that black carbon emitted from biomass burning could slightly warm the atmosphere (+0.52 W·m^{-2}) while causing slightly cooling at the surface (–0.73 W·m^{-2}) and the top of the atmosphere (–0.22 W·m^{-2}) over the Ross Sea.

Keywords **Australian fires**, **biomass burning**, **aerosol composition**, **climate effect**, **Ross Sea**

Citation: Chen A F, Wang L Q, Liu H W, et al. Characteristics of Antarctic aerosol composition during the Australian fires of 2019–2020. Adv Polar Sci, 2024, 35(4): 421-437, doi: 10.12429/j.advps.2024.0023

1 Introduction

Human activity is changing the global water cycle and carbon cycle (IPCC, 2019). Although drought risks associated with climate change vary by region, warming and drying will increase the risk of frequent and intense forest fires (Abatzoglou et al., 2019; Bowman et al., 2020; Huang et al., 2015). Wildfires, in turn, exert a stronger grip on the climate. Among them, wildfires alter radiative forcing at regional to global scales by releasing greenhouse gases and aerosols. Feedback between climate and wildfires is complex and often difficult to capture in climate models, resulting in a high degree of uncertainty in future projections (Tang et al., 2021). Although aerosols or photochemical compounds produced during biomass combustion have a large radiative impact on climate, they are still rarely quantified in the literature. This is especially true in the Southern Hemisphere, which has a smaller number of stations than in the Northern Hemisphere.

From September 2019 to March 2020, devastating bushfires occurred in Australia (Boer et al., 2020). The fire is on par with the five deadliest wildfires on record in Australia, with devastating ecological and social impacts, air quality and human health due to its proximity to major

* Corresponding author. ORCID: 0000-0003-1703-5157. E-mail: zqxie@ustc.edu.cn.

Australian residential areas and animal habitats. Fires have destroyed more than tens of thousands of hectares of forest, killed 451 people, killed approximately 1 billion animals and caused extensive property damage (Borchers Arriagada et al., 2020). Australian fires emit a large number of biomass aerosols and greenhouse gases (such as carbon dioxide (CO_2), methane (CH_4), etc.) and photochemical precursors that produce ozone (O_3), all of which have an impact on climate (Chang et al., 2021). Li et al. (2021) quantified the aerosols and greenhouse gases produced during Australian fires. The results showed that the fires burned 112.3 Tg of biomass and released 178.6±13.6 Tg of CO_2, 1.71±1.28 Tg particulate matter ($PM_{2.5}$) and 0.061± 0.04 Tg black carbon (BC).

Antarctica is often considered the most primitive continent on Earth, but it is subject to a variety of worrisome impacts at local to regional scales (Khan et al., 2019). A number of observations have been made in Antarctica over the past few decades, but these have focused on the impact of human activity on the Antarctic. Attention has been given to the effects of persistent organic pollutants on Antarctic ecology and BC produced by human activities on Antarctic climate, but less attention has been given to the effects of natural forest fires on Antarctic climate and environment (Hao et al., 2019; Hara et al., 2019; Khan et al., 2019; Morales et al., 2022). Projections show that based on current climate conditions, fires will become more frequent and more severe globally in the future (de Groot et al., 2013; Whitman et al., 2015), the impact of sudden fire events on the environment should not be underestimated, and researchers should pay more attention to the impact of forest fires on climate.

This paper reports the characteristics of aerosol components (mainly including organic components, inorganic water-soluble ions, organic carbon (OC) and elemental carbon (EC)) collected from the Ross Sea in Antarctic during the Australian fires of 2019–2020. The objective was to investigate the possible impacts of the 2019–2020 Australian fires on Antarctic aerosol fractions and their potential climate effects.

2 Methods

2.1 Study area and sampling

The aerosol samples (total suspended particulates, TSP) were collected in 2019–2020 during the 36th Chinese National Antarctic Research Expedition from the Ross Sea, Antarctic (Figure 1a). A high-volume air sampler, which was installed on the bow deck of R/V *Xuelong*, was used to collect aerosol samples as well as field blanks. The atmosphere was filtered through a pre-cleaned quartz filter film. We collected 39 samples and the samples were sealed and stored in the refrigerator at –20 ℃ until analysis. The total sampling time was approximately 24 h, and the sampling volume was approximately 1300 m^3. Details are shown in Table S1. In order to avoid pollution from ship exhaust as much as possible, we placed a high-volume sampler on the top deck of the ship and took samples while the ship was moving upwind. In addition, if the sample is contaminated by ship exhaust, the corresponding EC will be high. We analyzed the correlation between organic tracers and EC (Table S2) and found that there was no necessary connection between EC and organic tracers. In other words, our samples are basically not contaminated by ship exhaust.

2.2 Analysis of components

Arabitol, mannitol, levoglucosan (Lev) and its isomers (galactosan (Gan) and mannosan (Man)) were analyzed by GC-MS (Agilent 7890B-5977B, EI mode, HP-5). Details were shown in Chen et al. (2022). Briefly, one quarter of each quartz filter film was used for Lev and its isomers analysis. Components were extracted by an accelerated solvent extraction device (ASE 350, Thermo Fisher Scientific), and then the solution was concentrated, blow-dried and silanized at 70 ℃ for 1 h, finally, the solution was detected by GC-MS. Ion chromatography was used to detect water-soluble ions (SO_4^{2-}, NO_3^-, Cl^-, Ca^{2+}, Na^+, K^+, Mg^{2+} and NH_4^+). In addition, OC/EC was analyzed using a 2015 multiband thermal/optical method Carbon Morphology Analyzer (DRI Model 2015). Each test included at least two reagent blanks, two field blanks, and one for the recovery test. The recovery rate of all samples was between 90% and 110%. The average recoveries of Lev and its isomers from spiked anhydrous sodium sulfate (n = 4) ranged from 72% to 99%. The method detection limits (MDLs) were 4.67–27.77 ng per sample for Lev and their isomers (means of field blanks plus three times the standard deviations).

2.3 Backward trajectory and SBDART model

Online HYSPLIT (http://ready.arl.noaa.gov/HYSPLIT.php) was used to retrieve the backward trajectory of air mass. According to the lifetime of Lev in the atmosphere calculated by Fraser and Lakshmanan (2000), 10-day backward trajectories were calculated at 100 m above the sampling site. SBDART was used to simulate the shortwave radiative forcing of light-absorbing aerosols (Pu et al., 2019; Yuan et al., 2021; Zhao et al., 2019). Aerosol optical depth (AOD), single scattering albedo (SSA), and metronomic parameter (g) were needed. We obtained AOD and SSA data from the Aerosol Robotic Network (AERONET) website (https://aeronet.gsfc.nasa.gov/). The total aerosol radiative forcing was calculated by AOD data from the Marambio site near the Ross Sea. The light absorption coefficient for BC (b_{BC}) was calculated from the measured BC mass concentration using a mass absorption cross-section (MAC) of 10.0 $m^2 \cdot g^{-1}$ at 660 nm and an absorption Ångström exponent (AAE) of 1 to compute the absorption at other wavelengths. Text S1 shows the calculation formula of b_{BC}, AOD of BC aerosols, and SSA.

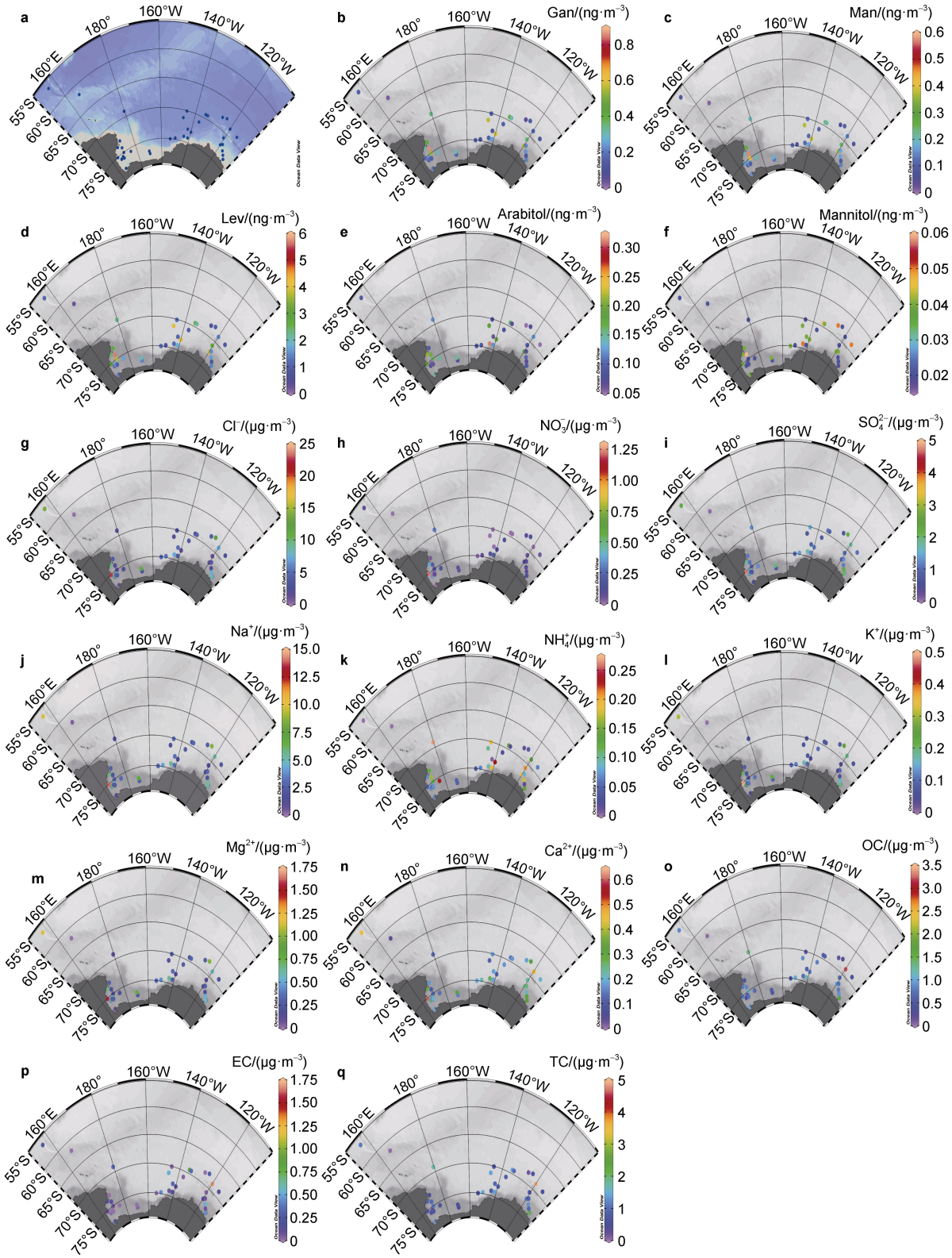

Figure 1 Location map and concentrations of different components. **a**, sampling locations; **b**, the concentrations of Gan; **c**, the concentrations of Man; **d**, the concentrations of Lev; **e**, the concentrations of arabitol; **f**, the concentrations of mannitol; **g**, the concentrations of Cl^-; **h**, the concentrations of NO_3^-; **i**, the concentrations of SO_4^{2-}; **j**, the concentrations of Na^+; **k**, the concentrations of NH_4^+; **l**, the concentrations of K^+; **m**, the concentrations of Mg^{2+}; **n**, the concentrations of Ca^{2+}; **o**, the concentrations of OC; **p**, the concentrations of EC; **q**, the concentrations of total carbon (TC).

The radiative forcing of BC was estimated by subtracting aerosols other than BC from total aerosols. Detail parameters, such as AOD, and solar zenith angle (SZA) were shown in Table S3.

3 Results and discussion

3.1 Aerosol compositions characteristics and sources

The ion observation results of this study are approximately 10 times the observation results of Zhongshan Station in Antarctica from 2005 to 2008 (Xu et al., 2019). The average mass concentrations of these components are distributed as follows (from highest to lowest): Cl^-, Na^+, SO_4^{2-}, OC, Mg^{2+}, Ca^{2+}, EC, K^+, NO_3^- and NH_4^+. Cl^- and Na^+ were dominant, with concentrations of 5.06±4.45 and 3.60±2.67 μg·m^{-3}, respectively. The dominant distribution pattern is consistent with previous observations at Zhongshan Station in Antarctica (Xu et al., 2019) but inconsistent with Barbaro et al. (2017) observations, which indicate that the dominant ions are SO_4^{2-}, Mg^{2+}, Na^+ and Cl^-. The different distribution patterns may be related to the different particle sizes of the collected samples. Barbaro et al. (2016) and Xu et al. (2021) showed that the distribution patterns of water-soluble ions in different particle sizes were different; Cl^-, Na^+ and Mg^{2+} were more likely to occur on coarse particles (1–10 μm), while NH_4^+, NO_3^- and K^+ were more likely to occur on fine particles (<1 μm). Cl^- and Na^+ are important components of the ocean, which may imply that the collected samples are mainly affected by marine sources.

Lev, Gan and Man are specific compounds for cellulose or hemicellulose that burn at a temperature range of 150–350 ℃. Throughout the entire sampling period, the concentrations of Lev, Gan and Man were 0.23 to 5.65 ng·m^{-3} (with an average of 1.90 ng·m^{-3}), 0.01 to 0.57 ng·m^{-3} (with an average of 0.18 ng·m^{-3}), and 0.02 to 0.86 ng·m^{-3} (with an average of 0.26 ng·m^{-3}), respectively. Lev was dominant (81.1%), followed by Man (11.2%) and Gan (7.7%). This distribution pattern is similar to many previous studies (van Drooge et al., 2014; Zhu et al., 2015). In addition, the observation results are of the same magnitude as that of Hu et al. (2013), while due to the distance from biomass burning sources and barriers of Antarctic marginal seas, the results which were observed in polar marine are higher than those observed in Antarctic plateau (Zangrando et al., 2016). This value is much lower than some terrestrial observations (Galindo et al., 2021; Zheng et al., 2018). Arabitol and mannitol are organic tracers of fungi in the atmosphere (Samaké et al., 2019). Bauer et al. (2008) found that arabitol and mannitol concentrations were well correlated with the number of fungal spores. Both of them can be used to estimate the contribution of biogenic aerosols to overall organic aerosols. In this study, arabitol was detected more frequently than mannitol, with the concentration of mannitol falling below the detection limit in over half of the samples, while arabitol exhibited a higher concentration compared to mannitol. Compared with other research results (Liang et al., 2013; Yttri et al., 2007; Zhang et al., 2010), this study is at a low level. Yttri et al. (2007) showed that the annual average concentrations of arabitol and mannitol in rural Norway were 0.42 and 0.27 ng·m^{-3}, respectively. Liang et al. (2013) found that the annual average concentrations of arabitol and mannitol in Beijing, China, were 7.4 and 10.3 ng·m^{-3}, respectively. Zhang et al. (2010) also observed high concentrations of arabitol and mannitol (7.0 and 16.0 ng·m^{-3}) at a mountain site in southern China. These comparative analyses might indicate that the biological diversity of Antarctica is lower than that observed in urban and rural ecosystems.

SPSS 19.0 software was used for the principal component analysis (PCA). To facilitate the interpretation of the factors extracted by PCA, Varimax was used to rotate each factor. Factors with eigenvalues greater than 1 are extracted. Table 1 shows the loading of each factor extracted by PCA. PCA extracted four components that explained 86.3% of the total variance.

Table 1 Varimax-rotated factor loadings of PCA[a]

	PC1	PC2	PC3
Gan	–0.156	**0.954**	–0.028
Man	–0.148	**0.955**	–0.022
Lev	–0.005	**0.967**	–0.037
Arabitol	0.272	0.706	0.129
Cl^-	**0.972**[b]	–0.164	–0.041
NO_3^-	0.762	0.238	–0.14
SO_4^{2-}	**0.955**	0.084	0.093
Na^+	**0.978**	–0.117	0.022
NH_4^+	–0.246	0.657	0.283
K^+	**0.983**	–0.108	0.05
Mg^{2+}	**0.965**	–0.172	0.006
Ca^{2+}	**0.885**	–0.126	0.317
OC	0.104	0.182	**0.922**
EC	0.018	–0.014	**0.918**
Variance	46.1%	27.1%	13.1%
Cumulative	46.1%	73.2%	86.3%

Notes: [a], The PCA is based on Eigenvalues >1 and Varimax rotation. [b], The scores that are also referred to as loadings, suggest that the variation within the respective element items significantly contributes to the overall variance captured by the principal component (PC). Bold font indicates environmental parameters with major contributions.

PC1 accounted for 46.1% of the overall variance, encompassing primarily Cl^-, SO_4^{2-}, Na^+, K^+, Mg^{2+}, and Ca^{2+}. It is noteworthy that the majority of constituent ions in PC1, exceeding 90%, are Cl^- and Na^+, which are key components of sea salt (Yoshizue et al., 2019), while the remaining ions originate mainly from the ocean. Thus, PC1 predominantly

signifies the influence of marine sources on aerosols. PC2, responsible for 27.1% of the total variance, primarily consists of Lev and its isomers, collectively indicating biomass burning as the source of the aerosol component. PC3, accounting for 13.1% of the total variance, is characterized by OC and EC, suggesting that aerosols might also be influenced by additional organic constituents. The PCA results reveal that aerosol components in the Ross Sea region of the Southern Ocean are contributed not only by local sources but also by the long-range transport of organic materials. Furthermore, based on the variance explained by each component, sea salt contributes most significantly to the aerosol composition, followed by biomass burning, and additionally, other organic components also play a role.

The findings of this study align well with earlier observations. Research conducted by Barbaro et al. (2016) in Terra Nova Bay, Victoria Land, Antarctica, similarly indicates that a substantial portion of aerosol fractions are influenced by sea salt, with elevated levels of Cl^- and Na^+. Furthermore, numerous studies have demonstrated that long-distance transport carries organic components from lower and middle latitudes to the high latitudes of Antarctica, thereby impacting the atmospheric composition in that region (Antony et al., 2014; Deng et al., 2021; Shi et al., 2019). Specifically, Shi et al. (2019) identified levoglucan, vanillic acid, and syringic acid in the ice and snow across the East Antarctic ice sheet, which are believed to originate primarily from biomass burning in the Southern Hemisphere's land areas. Antony et al. (2014) also discovered that certain organic components in the Antarctic ice sheet mainly arrive through long-distance transport. Additionally, Deng et al. (2021) found that marine emissions potentially impact bioorganic aerosols in the Antarctic Peninsula.

3.2 Potential source areas for biomass burning

The composition analysis in Section 3.1 shows that the samples collected in the study area are affected by biomass burning. These biomarkers of biomass burning may be mainly derived from Southern Hemisphere continents (e.g., Australia, South America and South Africa) (Chen et al., 2022; Hu et al., 2013). To determine the specific source area, the backward trajectory of the collected samples were drawn (Figure 2). As shown in Figure 2, in most cases, the air mass was not directly derived from any other continent within the 10-day period but traveled circuitously around West Antarctica and the Southern Ocean (most of the air mass trajectories were less than 2 km altitude). This result is probably caused by the relatively long duration of Lev transport to Antarctica. The long lifetime of Lev in the atmosphere allows homogeneous mixing of this compound from multiple sources. Hence, the Lev detected in Ross Sea reflects a mixed signal of fire activities in the Southern Hemisphere, in which Australia and South America are probably the most important source areas of fire.

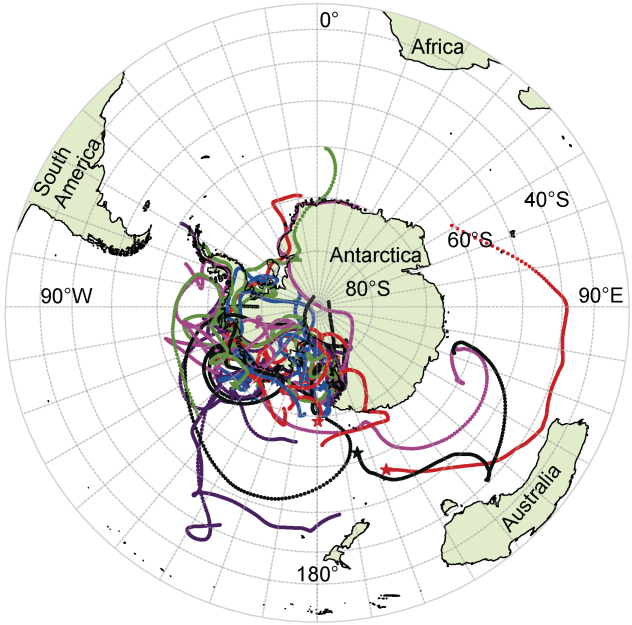

Figure 2 Sample backward trajectories. Stars are the average sampling locations, dotted lines are 10-days air mass backward trajectories at 100 m above sea level.

Figure 3 shows the ratios of Lev and its isomers in all samples. The C_{Lev}/C_{Man} of most samples was in the range of 8–14, and the C_{Lev}/C_{Man} of only two sample points was approximately 18, while the ratio of the C_{Man}/C_{Gan} ratio in all samples was less than 1, concentrated in the range of 0.5–0.9. Previous studies have shown that the ratio of C_{Lev}/C_{Man} ranges from 0 to 5, the ratio of C_{Man}/C_{Gan} ranges from 0.6 to 3 during softwood combustion (Engling et al., 2006; Kuo et al., 2011), and the C_{Lev}/C_{Man} and C_{Man}/C_{Gan} ratios of grass and pine needles were 5.0–10.0 and 0.2–1.0, respectively (Engling et al., 2006; Kuo et al., 2011; Schmidl et al., 2008a). For hardwood combustion, the C_{Lev}/C_{Man} ratio ranges from 10.0 to 30.0, and the ratio of C_{Man}/C_{Gan} is approximately 0.6–3.0 (Engling et al., 2006; Schmidl et al., 2008b); in addition, the C_{Lev}/C_{Man} values of crop residues are usually greater than 40 (Zhang et al., 2007). Lev is significantly correlated with Man and Gan (the r values were 0.98 and 0.97, respectively, $p < 0.01$), which indicates that these compounds may have experienced the same transport and deposition processes (Dietze et al., 2020). The ratio thus may minimize the impact of degradation during transport. Based on the comparison between the data of this study and previous studies, it can be found that the ratio of this study mainly fell in the range of hardwood and grass, which implies that the samples were mainly affected by fires, and the vegetation system was composed mainly of hardwood and grass.

The C_{Lev}/C_{Man} ratios in this study are higher than some previously reported values which were detected in South America (Dietze et al., 2020; Kirchgeorg et al., 2014; Schreuder et al., 2019; Schüpbach et al., 2015), suggesting

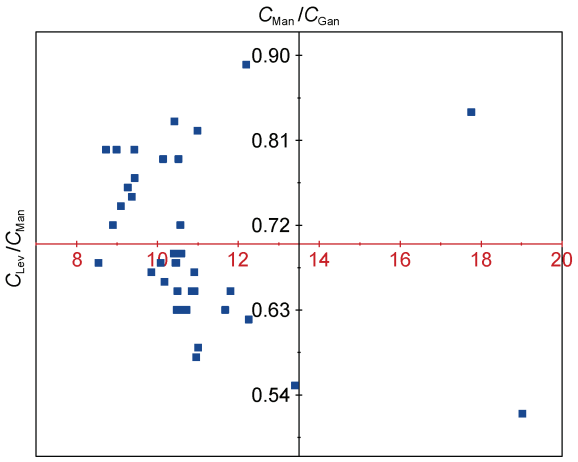

Figure 3 Ratio of Lev and its isomers. The red coordinate axis represents the value of C_{Lev}/C_{Man}, while the black coordinate axis represents the value of C_{Man}/C_{Gan}.

that the burning vegetation in South America is dominated by softwood. Studies have shown that the ecosystem of tropical northern Australia is dominated by grasslands (Mallet et al., 2017a), southeastern Australia is dominated by forest and grassland ecosystems (Cruz et al., 2012). The major fuel groups for bushfires encompass Acacia shrublands, Mallee woodlands and shrublands, Chenopod shrubs, Samphire shrubs and forb-dominated communities, Hummock grasslands, Tussock grasslands, open woodlands, low closed forests and closed shrublands, rainforests and vine thickets, Eucalypt open forests, Eucalypt tall open forests, and Eucalypt low open forests (Russell-Smith et al., 2007).

In addition, Kloss et al. (2021) demonstrated that through satellite, ground remote sensing and field observations, Australian fires had a significant impact on the Southern Hemisphere atmosphere, and amounts of material from fires are transported up into the troposphere and then transported over long distances. Pope et al. (2021) analyzed trace gas emissions from Australian fires and their long-range transport using state-of-the-art near-real-time satellite measurements of tropospheric composition. Observations suggest that the apparent fire plume from the Australian fires managed to circle the entire Southern Hemisphere in a matter of weeks and spread eastward to the South Pacific Ocean, South America, South Atlantic Ocean, Africa, and the Indian Ocean. Therefore, it is concluded that the aerosol samples collected in the Ross Sea of Antarctic may mainly affected by biomass burning in Australia. However, the contribution from South America cannot be ruled out.

3.3 Potential climatic effects of biomass burning

Forest fires release BC and aerosols into the atmosphere, imposing significant impacts on regional and even global climates (Feltracco et al., 2020; Mallet et al., 2017b; Zangrando et al., 2016). To assess the potential climate impact of Australian fires on the Ross Sea, we used SBDART to estimate the direct radiative effect (DRE) of BC. BC, which is released from biomass burning, used in this study was calculated by the ratio of Lev to total and organic carbon released by forest fires observed in previous studies (Saarikoski et al., 2007; Yttri et al., 2014) and the Lev concentration measured in the Ross Sea (details was shown in Text S2). Because of the photooxidation of Lev during long-distance transport, it may underestimate the BC from biomass burning. However, it can evaluate the minimum impact of Australian fires on the Ross Sea environment.

The output parameters of the SBDART model mainly include total downward flux and total upward flux at the top of the atmosphere (TOPDN and TOPUP), total downward flux and total upward flux at the surface (BOTDN and BOTUP). The DRE values at the top of the atmosphere (TOA) were calculated by subtracting TOPUP from TOPDN, the DRE values at the surface (SUF) were calculated by subtracting BOTUP from BOTDN, the DRE values at the atmosphere (ATM) were calculated by subtracting SUF from TOA. Figure 4 shows the DRE values for all samples. The mean DRE value at the ATM is 0.52±0.48 $W{\cdot}m^{-2}$, while those at the TOA and at the SUF are −0.22±0.26 $W{\cdot}m^{-2}$ and −0.73±0.39 $W{\cdot}m^{-2}$, respectively. These results may indicate that Australian fires have a potential weak warming and heating effect on the Antarctic (Ross Sea) atmosphere, while they may have a potential cooling effect on the surface and the upper atmosphere. The results are similar to previous studies showing that BC aerosols have a significant radiative heating effect on the atmosphere and cooling effect on the surface. Chang et al. (2021) showed that aerosols generated by biomass burning

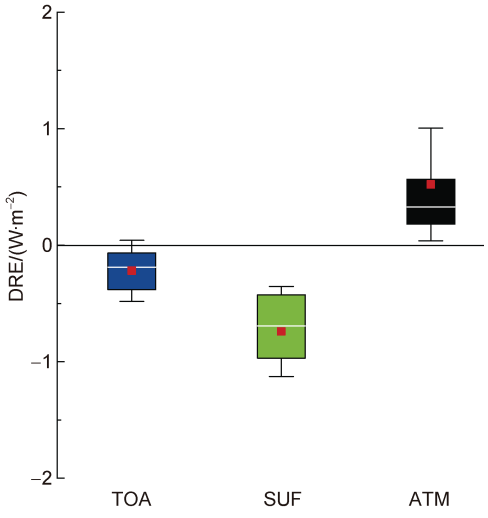

Figure 4 Radiative effect due to BC aerosols at the TOA, SUF and ATM in the Antarctic. For each box plot shows the 25th and 75th percentiles, the median is the 50th percentile and is represented by a white line, error bars represent one standard deviation and the small red block in each box represents the mean value of radiative effect.

in Australia caused a significant cooling effect at the top of the atmosphere in the Australian region, with radiative forcing ranging from –14.8 to –17.7 $W \cdot m^{-2}$. In addition, Devara et al. (2011) observed aerosol optical thickness at Maitri Station in Antarctica from 2004 to 2005 and calculated the radiative forcing of aerosols, and the results showed that the radiative forcing of aerosols on the surface reached –0.47 $W \cdot m^{-2}$.

It is worth noting that some uncertainties exist in the calculation of DRE. These uncertainties include the model itself and data input to the model. SBDART is mainly used to study local (point) radiative effect, and the overall uncertainty of the radiative effect value can reach 15% due to bias in SBDART simulation (Alam et al., 2012). In addition, the BC aerosol profile, which was input to the model, was inferred based on the observed Lev data and BC aerosol profile observed by aircraft in another study. Samset et al. (2013) showed that in DRE calculations, the vertical profile data of BC can cause at least 20% uncertainty. Although there is some uncertainty in this estimate, it can still provide a reference for subsequent research. As an increasing number of intense fires are expected to occur globally due to climate change, attention should be given to the direct radiation effects of aerosols released by forest fires (de Groot et al., 2013; Whitman et al., 2015).

4 Conclusion

This study examined the chemical composition of aerosols, potential source regions, and potential climatic impacts of Lev, its isomers, and water-soluble ions in TSP collected from the Ross Sea in Antarctic. The results of the PCA revealed that these components primarily originated from sea salt, biomass burning, and various organic constituents. Additionally, the analysis of backward trajectories and the ratios of C_{Lev}/C_{Man} and C_{Man}/C_{Gan} suggested Australia as a likely source region for biomass burning. Estimations using the SBDART model indicated that biomass burning in Australia could potentially lead to regional weak warming of the Antarctic atmosphere and cooling of the Antarctic surface.

Acknowledgments This work was supported by the National Natural Science Foundation of China (Grant nos. 41941014 and 41930532) and was financially supported by National Polar Special Program "Impact and Response of Antarctic Seas to Climate Change" (Grant no. IRASCC 01-01-02E). We thank the Chinese Arctic and Antarctic Administration, and Polar Research lnstitute of China for fieldwork support. We appreciate the anonymous reviewers and Associate Editor Dr. Sheeba Chenoli for their helpful comments.

References

Abatzoglou J T, Williams A P, Barbero R. 2019. Global emergence of anthropogenic climate change in fire weather indices. Geophys Res Lett, 46(1): 326-336, doi:10.1029/2018gl080959.

Alam K, Trautmann T, Blaschke T, et al. 2012. Aerosol optical and radiative properties during summer and winter seasons over Lahore and Karachi. Atmos Environ, 50: 234-245, doi:10.1016/j.atmosenv.2011.12.027.

Antony R, Grannas A M, Willoughby A S, et al. 2014. Origin and sources of dissolved organic matter in snow on the East Antarctic ice sheet. Environ Sci Technol, 48(11): 6151-6159, doi:10.1021/es405246a.

Barbaro E, Zangrando R, Kirchgeorg T, et al. 2016. An integrated study of the chemical composition of Antarctic aerosol to investigate natural and anthropogenic sources. Environ Chem, 13(5): 867-876, doi:10.1071/en16056.

Barbaro E, Zangrando R, Padoan S, et al. 2017. Aerosol and snow transfer processes: an investigation on the behavior of water-soluble organic compounds and ionic species. Chemosphere, 183: 132-138, doi:10.1016/j.chemosphere.2017.05.098.

Bauer H, Claeys M, Vermeylen R, et al. 2008. Arabitol and mannitol as tracers for the quantification of airborne fungal spores. Atmos Environ, 42(3): 588-593, doi:10.1016/j.atmosenv.2007.10.013.

Boer M M, Resco de Dios V, Bradstock R A. 2020. Unprecedented burn area of Australian mega forest fires. Nat Clim Change, 10: 171-172, doi:10.1038/s41558-020-0716-1.

Borchers Arriagada N, Palmer A J, Bowman D M, et al. 2020. Unprecedented smoke-related health burden associated with the 2019–20 bushfires in eastern Australia. Med J Aust, 213(6): 282-283, doi:10.5694/mja2.50545.

Bowman D M J S, Kolden C A, Abatzoglou J T, et al. 2020. Vegetation fires in the anthropocene. Nat Rev Earth Environ, 1: 500-515, doi:10.1038/s43017-020-0085-3.

Chang D Y, Yoon J, Lelieveld J, et al. 2021. Direct radiative forcing of biomass burning aerosols from the extensive Australian wildfires in 2019–2020. Environ Res Lett, 16(4): 044041, doi:10.1088/1748-9326/abecfe.

Chen A, Yang L, Kang H, et al. 2022. Southern hemisphere fire history since the late glacial, reconstructed from an Antarctic sediment core. Quat Sci Rev, 276: 107300, doi:10.1016/j.quascirev.2021.107300.

Cruz M G, Sullivan A L, Gould J S, et al. 2012. Anatomy of a catastrophic wildfire: the Black Saturday Kilmore East fire in Victoria, Australia. For Ecol Manag, 284: 269-285, doi:10.1016/j.foreco.2012.02.035.

de Groot W J, Flannigan M D, Cantin A S. 2013. Climate change impacts on future boreal fire regimes. For Ecol Manag, 294: 35-44, doi:10.1016/j.foreco.2012.09.027.

Deng J, Gao Y, Zhu J, et al. 2021. Molecular markers for fungal spores and biogenic SOA over the Antarctic Peninsula: field measurements and modeling results. Sci Total Environ, 762: 143089, doi:10.1016/j.scitotenv.2020.143089.

Devara P C S, Sonbawne S M, Dani K K, et al. 2011. Characterization of aerosols and pre-cursor gases over Maitri during 24th Indian Antarctica Expedition. Int J Remote Sens, 32(20): 5815-5826, doi:10.1080/01431161.2010.507681.

Dietze E, Mangelsdorf K, Andreev A, et al. 2020. Relationships between low-temperature fires, climate and vegetation during three late glacials and interglacials of the last 430 kyr in northeastern Siberia reconstructed from monosaccharide anhydrides in Lake El'gygytgyn sediments. Clim Past, 16(2): 799-818, doi:10.5194/cp-16-799-2020.

Engling G, Carrico C M, Kreidenweis S M, et al. 2006. Determination of

levoglucosan in biomass combustion aerosol by high-performance anion-exchange chromatography with pulsed amperometric detection. Atmos Environ, 40: 299-311, doi:10.1016/j.atmosenv.2005.12.069.

Feltracco M, Barbaro E, Tedeschi S, et al. 2020. Interannual variability of sugars in Arctic aerosol: biomass burning and biogenic inputs. Sci Total Environ, 706: 136089, doi:10.1016/j.scitotenv.2019.136089.

Fraser M P, Lakshmanan K. 2000. Using levoglucosan as a molecular marker for the long-range transport of biomass combustion aerosols. Environ Sci Technol, 34(21): 4560-4564, doi:10.1021/es991229l.

Galindo N, Clemente Á, Yubero E, et al. 2021. PM_{10} chemical composition at a residential site in the western Mediterranean: estimation of the contribution of biomass burning from levoglucosan and its isomers. Environ Res, 196: 110394, doi:10.1016/j.envres.2020.110394.

Hao Y, Li Y, Han X, et al. 2019. Air monitoring of polychlorinated biphenyls, polybrominated diphenyl ethers and organochlorine pesticides in West Antarctica during 2011–2017: concentrations, temporal trends and potential sources. Environ Pollut, 249: 381-389, doi:10.1016/j.envpol.2019.03.039.

Hara K, Sudo K, Ohnishi T, et al. 2019. Seasonal features and origins of carbonaceous aerosols at Syowa Station, coastal Antarctica. Atmos Chem Phys, 19(11): 7817-7837, doi:10.5194/acp-19-7817-2019.

Hu Q H, Xie Z Q, Wang X M, et al. 2013. Levoglucosan indicates high levels of biomass burning aerosols over oceans from the Arctic to Antarctic. Sci Rep, 3: 3119, doi:10.1038/srep03119.

Huang Y, Wu S, Kaplan J O. 2015. Sensitivity of global wildfire occurrences to various factors in the context of global change. Atmos Environ, 121: 86-92, doi:10.1016/j.atmosenv.2015.06.002.

IPCC. 2019. Climate change and land: an IPCC special report on climate change, desertification, land degradation, sustainable land management, food security, and greenhouse gas fluxes in terrestrial ecosystems. https://www.ipcc.ch/srccl/.

Khan A L, Klein A G, Katich J M, et al. 2019. Local emissions and regional wildfires influence refractory black carbon observations near Palmer Station, Antarctica. Front Earth Sci, 7: 49, doi:10.3389/feart.2019.00049.

Kirchgeorg T, Schüpbach S, Kehrwald N, et al. 2014. Method for the determination of specific molecular markers of biomass burning in lake sediments. Org Geochem, 71: 1-6, doi:10.1016/j.orggeochem.2014.02.014.

Kloss C, Sellitto P, von Hobe M, et al. 2021. Australian fires 2019–2020: tropospheric and stratospheric pollution throughout the whole fire season. Front Environ Sci, 9: 652024, doi:10.3389/fenvs.2021.652024.

Kuo L J, Louchouarn P, Herbert B E. 2011. Influence of combustion conditions on yields of solvent-extractable anhydrosugars and lignin phenols in chars: implications for characterizations of biomass combustion residues. Chemosphere, 85(5): 797-805, doi:10.1016/j.chemosphere.2011.06.074.

Li F, Zhang X, Kondragunta S. 2021. Highly anomalous fire emissions from the 2019–2020 Australian bushfires. Environ Res Commun, 3(10): 105005, doi:10.1088/2515-7620/ac2e6f.

Liang L, Engling G, He K, et al. 2013. Evaluation of fungal spore characteristics in Beijing, China, based on molecular tracer measurements. Environ Res Lett, 8(1): 014005, doi:10.1088/1748-9326/8/1/014005.

Mallet M D, Desservettaz M J, Miljevic B, et al. 2017a. Biomass burning emissions in North Australia during the early dry season: an overview of the 2014 SAFIRED campaign. Atmos Chem Phys, 17(22): 13681-13697, doi:10.5194/acp-17-13681-2017.

Mallet M D, Cravigan L T, Milic A, et al. 2017b. Composition, size and cloud condensation nuclei activity of biomass burning aerosol from northern Australian savannah fires. Atmos Chem Phys, 17(5): 3605-3617, doi:10.5194/acp-17-3605-2017.

Morales P, Roscales J L, Muñoz-Arnanz J, et al. 2022. Evaluation of PCDD/Fs, PCBs and PBDEs in two penguin species from Antarctica. Chemosphere, 286: 131871, doi:10.1016/j.chemosphere.2021.131871.

Pope R J, Kerridge B J, Siddans R, et al. 2021. Large enhancements in Southern Hemisphere satellite-observed trace gases due to the 2019/2020 Australian wildfires. J Geophys Res Atmos, 126(18): e2021jd034892, doi:10.1029/2021jd034892.

Pu W, Cui J, Shi T, et al. 2019. The remote sensing of radiative forcing by light-absorbing particles (LAPs) in seasonal snow over northeastern China. Atmos Chem Phys, 19(15): 9949-9968, doi:10.5194/acp-19-9949-2019.

Russell-Smith J, Yates C P, Whitehead P J, et al. 2007. Bushfires 'down under': patterns and implications of contemporary Australian landscape burning. Int J Wildland Fire, 16(4): 361-377, doi:10.1071/wf07018.

Saarikoski S, Sillanpää M, Sofiev M, et al. 2007. Chemical composition of aerosols during a major biomass burning episode over northern Europe in spring 2006: experimental and modelling assessments. Atmos Environ, 41(17): 3577-3589, doi:10.1016/j.atmosenv.2006.12.053.

Samaké A, Jaffrezo J L, Favez O, et al. 2019. Arabitol, mannitol, and glucose as tracers of primary biogenic organic aerosol: the influence of environmental factors on ambient air concentrations and spatial distribution over France. Atmos Chem Phys, 19(16): 11013-11030.

Samset B H, Myhre G, Schulz M, et al. 2013. Black carbon vertical profiles strongly affect its radiative forcing uncertainty. Atmos Chem Phys, 13(5): 2423-2434, doi:10.5194/acp-13-2423-2013.

Schmidl C, Bauer H, Dattler A, et al. 2008a. Chemical characterisation of particle emissions from burning leaves. Atmos Environ, 42(40): 9070-9079, doi:10.1016/j.atmosenv.2008.09.010.

Schmidl C, Marr I L, Caseiro A, et al. 2008b. Chemical characterisation of fine particle emissions from wood stove combustion of common woods growing in mid-European Alpine regions. Atmos Environ, 42(1): 126-141, doi:10.1016/j.atmosenv.2007.09.028.

Schreuder L T, Hopmans E C, Castañeda I S, et al. 2019. Late Quaternary biomass burning in Northwest Africa and interactions with climate, vegetation, and humans. Paleoceanog Paleoclimatol, 34(2): 153-163, doi:10.1029/2018pa003467.

Schüpbach S, Kirchgeorg T, Colombaroli D, et al. 2015. Combining charcoal sediment and molecular markers to infer a Holocene fire history in the Maya Lowlands of Petén, Guatemala. Quat Sci Rev, 115: 123-131, doi:10.1016/j.quascirev.2015.03.004.

Shi G T, Wang X C, Li Y S, et al. 2019. Organic tracers from biomass burning in snow from the coast to the ice sheet summit of East Antarctica. Atmos Environ, 201: 231-241, doi:10.1016/j.atmosenv.2018.12.058.

Tang W, Llort J, Weis J, et al. 2021. Widespread phytoplankton blooms triggered by 2019–2020 Australian wildfires. Nature, 597: 370-375, doi:10.1038/s41586-021-03805-8.

van Drooge B L, Fontal M, Bravo N, et al. 2014. Seasonal and spatial variation of organic tracers for biomass burning in PM_1 aerosols from highly insolated urban areas. Environ Sci Pollut Res Int, 21(20): 11661-11670, doi:10.1007/s11356-014-2545-0.

Whitman E, Sherren K, Rapaport E. 2015. Increasing daily wildfire risk in the Acadian Forest Region of Nova Scotia, Canada, under future climate change. Reg Environ Change, 15(7): 1447-1459, doi:10.1007/s10113-014-0698-5.

Xu G, Chen L, Zhang M, et al. 2019. Year-round records of bulk aerosol composition over the Zhongshan Station, Coastal East Antarctica. Air Qual Atmos Health, 12(3): 271-288, doi:10.1007/s11869-018-0642-9.

Xu G, Chen L, Xu T, et al. 2021. Distributions of water-soluble ions in size-aggregated aerosols over the Southern Ocean and coastal Antarctica. Environ Sci Proc Imp, 23(9): 1316-1327, doi:10.1039/D1EM00089F.

Yoshizue M, Iwamoto Y, Adachi K, et al. 2019. Individual particle analysis of marine aerosols collected during the North–South transect cruise in the Pacific Ocean and its marginal seas. J Oceanogr, 75(6): 513-524, doi:10.1007/s10872-019-00519-4.

Yttri K E, Dye C, Kiss G. 2007. Ambient aerosol concentrations of sugars and sugar-alcohols at four different sites in Norway. Atmos Chem Phys, 7(16): 4267-4279, doi:10.5194/acp-7-4267-2007.

Yttri K E, Lund Myhre C, Eckhardt S, et al. 2014. Quantifying black carbon from biomass burning by means of levoglucosan–a one-year time series at the Arctic Observatory Zeppelin. Atmos Chem Phys, 14(12): 6427-6442, doi:10.5194/acp-14-6427-2014.

Yuan Q, Xu J, Liu L, et al. 2021. Evidence for large amounts of brown carbonaceous tarballs in the Himalayan atmosphere. Environ Sci Technol Lett, 8(1): 16-23, doi:10.1021/acs.estlett.0c00735.

Zangrando R, Barbaro E, Vecchiato M, et al. 2016. Levoglucosan and phenols in Antarctic marine, coastal and plateau aerosols. Sci Total Environ, 544: 606-616, doi:10.1016/j.scitotenv.2015.11.166.

Zhang T, Engling G, Chan C Y, et al. 2010. Contribution of fungal spores to particulate matter in a tropical rainforest. Environ Res Lett, 5(2): 024010, doi:10.1088/1748-9326/5/2/024010.

Zhang Y X, Shao M, Zhang Y H, et al. 2007. Source profiles of particulate organic matters emitted from cereal straw burnings. J Environ Sci, 19(2): 167-175, doi:10.1016/S1001-0742(07)60027-8.

Zhao S, Yu Y, Yin D, et al. 2019. Concentrations, optical and radiative properties of carbonaceous aerosols over urban Lanzhou, a typical valley city: results from *in situ* observations and numerical model. Atmos Environ, 213: 470-484, doi:10.1016/j.atmosenv.2019.06.046.

Zheng L, Yang X, Lai S, et al. 2018. Impacts of springtime biomass burning in the northern Southeast Asia on marine organic aerosols over the Gulf of Tonkin, China. Environ Pollut, 237: 285-297, doi:10.1016/j.envpol.2018.01.089.

Zhu C, Kawamura K, Kunwar B. 2015. Effect of biomass burning over the western North Pacific Rim: wintertime maxima of anhydrosugars in ambient aerosols from Okinawa. Atmos Chem Phys, 15(4): 1959-1973, doi:10.5194/acp-15-1959-2015.

Supplementary Tables and Texts

Table S1 Sample information of Antarctic aerosol

Site	Latitude[a]	Longitude[a]	Air temperature/℃	Sampling time (YYYY-MM-DD)	Sampling volume[b]/m^3
2019-B1	56.42°N	157.01°E	6.7	2019-12-26–2019-12-27	1444
2019-B2	61.77°N	164.60°E	5.6	2019-12-27–2019-12-28	2410
2019-B3	67.83°N	123.94°W	2.2	2020-01-20–2020-01-21	1439
2019-B4	68.13°N	126.18°W	0.9	2020-02-02–2020-02-03	1464
2019-B5	68.84°N	120.08°W	1.8	2020-01-21–2020-01-22	1355
2019-B6	68.94°N	114.96°W	1.4	2020-01-31–2020-02-01	1456
2019-B7	69.01°N	179.64°E	3.3	2019-12-29–2019-12-30	1456
2019-B8	69.36°N	134.63°W	2.9	2020-01-19–2020-01-20	1239
2019-B9	69.36°N	133.55°W	–0.3	2020-02-03–2020-02-04	1349
2019-B10	70.05°N	145.20°W	1.8	2020-01-16–2020-01-17	1462
2019-B11	70.83°N	120.52°W	0.9	2020-01-22–2020-01-23	1470
2019-B12	71.00°N	136.95°W	1.4	2020-02-04–2020-02-05	1356
2019-B13	71.25°N	146.51°W	2.9	2020-01-18–2020-01-19	1433
2019-B14	71.76°N	119.06°W	0.9	2020-01-29–2020-01-30	1446
2019-B15	72.10°N	120.05°W	2.9	2020-01-23–2020-01-24	1458
2019-B16	72.59°N	117.09°W	1.4	2020-01-25-2020-01-26	1462
2019-B17	72.84°N	142.47°W	0.9	2020-02-05–2020-02-06	1384
2019-B18	73.02°N	171.19°E	1.1	2020-02-14–2020-02-15	1410
2019-B19	73.04°N	115.32°W	1.5	2020-01-28–2020-01-29	1415
2019-B20	73.10°N	139.90°W	5.0	2020-01-14–2020-01-15	1434
2019-B21	73.49°N	113.57°W	1.2	2020-01-26–2020-01-27	1397
2019-B22	73.55°N	113.76°W	0.6	2020-01-27–2020-01-28	1449
2019-B23	73.64°N	168.04°E	0.6	2020-02-10–2020-02-11	1450
2019-B24	74.16°N	170.60°E	4.5	2019-12-31–2019-01-01	1464
2019-B25	74.17°N	144.02°W	–0.1	2020-01-12–2020-01-13	1473
2019-B26	74.21°N	141.34°W	2.8	2020-01-13–2020-01-14	1443
2019-B27	74.76°N	149.97°W	–1.1	2020-01-10–2020-01-11	1465
2019-B28	75.00°N	170.26°E	3.9	2020-01-04–2020-01-05	1447
2019-B29	75.01°N	153.62°W	1.4	2020-02-06–2020-02-07	1418
2019-B30	75.04°N	164.83°E	–0.5	2020-02-09–2020-02-10	1355
2019-B31	75.48°N	168.53°E	–0.6	2020-02-15–2020-02-16	1384
2019-B32	75.54°N	175.29°E	1.6	2020-01-05–2020-01-06	1460
2019-B33	75.60°N	167.97°E	0.4	2020-02-21–2020-02-22	1368
2019-B34	75.68°N	166.96°E	–3.0	2020-02-20–2020-02-21	1479
2019-B35	75.70°N	166.56°E	–2.3	2020-02-18–2020-02-19	1241
2019-B36	75.79°N	168.84°E	0.4	2020-02-22–2020-02-23	1330
2019-B37	76.71°N	170.58°W	0.2	2020-02-07–2020-02-08	1446
2019-B38	77.16°N	170.22°W	–3.5	2020-01-08–2020-01-09	1499
2019-B39	77.36°N	166.08°E	–4.1	2020-01-07–2020-01-08	1502

Notes: “a” denotes the latitude and the longitude indicate the mean location of the start and end of each sampling episode; “b” denotes sampling volume for air.

Table S2 Pearson correlations (r) of OC, EC, organic tracer and inorganic ions

	Gan	Man	Lev	Arabitol	Mannitol	Cl^-	NO_3^-	SO_4^{2-}	Na^+	NH_4^+	K^+	Mg^{2+}	Ca^{2+}	OC	EC
Gan	1														
Man	0.99**	1													
Lev	0.97**	0.98**	1												
Arabitol	0.55**	0.54**	0.58**	1											
Mannitol	0.43**	0.40*	0.44**	0.46**	1										
Cl^-	–0.28	–0.27	–0.14	0.11	–0.06	1									
NO_3^-	0.03	0.05	0.20	0.32*	0.04	0.66**	1								
SO_4^{2-}	–0.09	–0.08	0.05	0.29	0.00	0.90**	0.76**	1							
Na^+	–0.24	–0.24	–0.11	0.18	–0.07	0.98**	0.64**	0.92**	1						
NH_4^+	0.56**	0.55**	0.52**	0.39*	–0.03	–0.40*	0.04	–0.05	–0.33*	1					
K^+	–0.25	–0.24	–0.11	0.19	–0.08	0.98**	0.69**	0.92**	0.98**	–0.30	1				
Mg^{2+}	–0.29	–0.28	–0.16	0.14	–0.07	0.99**	0.61**	0.89**	0.99**	–0.39*	0.98**	1			
Ca^{2+}	–0.26	–0.24	–0.12	0.15	–0.07	0.86**	0.55**	0.87**	0.88**	–0.21	0.89**	0.87**	1		
OC	0.12	0.14	0.14	0.25	–0.20	0.03	0.04	0.19	0.09	0.35*	0.13	0.06	0.37*	1	
EC	0.00	–0.01	0.00	0.10	–0.02	0.00	–0.13	0.08	0.06	0.13	0.07	0.05	0.26	0.75**	1

Notes: *, p<0.05; **, p<0.01.

Table S3 Aerosol optical depth and SZA used in this study

	AOD	440 nm	675 nm	870 nm	1020 nm	$AOD_{NO\text{-}BC}$	440 nm	675 nm	870 nm	1020 nm	SZA /(°)
	0–2 km	0.00882632	0.00374332	0.00292808	0.00181325	0–2 km	0.00858046	0.00358306	0.00280374	0.00170719	
	2–4 km	0.00515563	0.00218655	0.00171035	0.00105915	2–4 km	0.00488734	0.00201167	0.00157467	0.00094342	
2019-B1	4–6 km	0.00465132	0.00197267	0.00154305	0.00095555	4–6 km	0.00418067	0.00166587	0.00130502	0.00075252	64
	6–8 km	0.00489246	0.00207493	0.00162305	0.00100509	6–8 km	0.00410118	0.00155914	0.00122286	0.00066375	
	8–10 km	0.00752527	0.00319153	0.00249647	0.00154596	8–10 km	0.00690531	0.00278741	0.00218293	0.00127853	
	0–2 km	0.00882632	0.00374332	0.00292808	0.00181325	0–2 km	0.00877699	0.00371116	0.00290313	0.00179197	
	2–4 km	0.00515563	0.00218655	0.00171035	0.00105915	2–4 km	0.00510180	0.00215146	0.00168313	0.00103593	
2019-B2	4–6 km	0.00465132	0.00197267	0.00154305	0.00095555	4–6 km	0.00455689	0.00191111	0.00149529	0.00091481	54
	6–8 km	0.00489246	0.00207493	0.00162305	0.00100509	6–8 km	0.00473369	0.00197144	0.00154275	0.00093660	
	8–10 km	0.00752527	0.00319153	0.00249647	0.00154596	8–10 km	0.00740088	0.00311045	0.00243356	0.00149230	
	0–2 km	0.01723279	0.00879306	0.00576265	0.00383002	0–2 km	0.01701131	0.00864869	0.00565063	0.00373447	
	2–4 km	0.01006602	0.00513620	0.00336608	0.00223719	2–4 km	0.00982433	0.00497866	0.00324384	0.00213293	
2019-B3	4–6 km	0.00908140	0.00463380	0.00303682	0.00201835	4–6 km	0.00865741	0.00435742	0.00282239	0.00183546	61
	6–8 km	0.00955220	0.00487402	0.00319426	0.00212299	6–8 km	0.00883937	0.00440936	0.00283374	0.00181549	
	8–10 km	0.01469259	0.00749692	0.00491320	0.00326545	8–10 km	0.01413409	0.00713286	0.00463074	0.00302453	
	0–2 km	0.02375240	0.01420181	0.00926918	0.00626407	0–2 km	0.02365020	0.01413519	0.00921749	0.00621998	
	2–4 km	0.01387425	0.00829556	0.00541431	0.00365897	2–4 km	0.01376272	0.00822286	0.00535791	0.00361085	
2019-B4	4–6 km	0.01251713	0.00748412	0.00488471	0.00330106	4–6 km	0.01232146	0.00735658	0.00478575	0.00321666	62
	6–8 km	0.01316604	0.00787212	0.00513794	0.00347220	6–8 km	0.01283709	0.00765768	0.00497157	0.00333029	
	8–10 km	0.02025117	0.01210839	0.00790286	0.00534071	8–10 km	0.01999344	0.01194039	0.00777251	0.00522953	
	0–2 km	0.01451136	0.00691785	0.00457930	0.00286128	0–2 km	0.01420193	0.00671614	0.00442281	0.00272780	
	2–4 km	0.00847638	0.00404085	0.00267486	0.00167133	2–4 km	0.00813871	0.00382075	0.00250409	0.00152567	
2019-B5	4–6 km	0.00764725	0.00364559	0.00241322	0.00150785	4–6 km	0.00705489	0.00325946	0.00211363	0.00125232	63
	6–8 km	0.00804370	0.00383459	0.00253832	0.00158602	6–8 km	0.00704779	0.00318540	0.00203465	0.00115641	
	8–10 km	0.01237231	0.00589812	0.00390429	0.00243951	8–10 km	0.01159203	0.00538949	0.00350966	0.00210292	

Continued

	AOD	440 nm	675 nm	870 nm	1020 nm	$AOD_{NO\text{-}BC}$	440 nm	675 nm	870 nm	1020 nm	SZA /(°)
	0–2 km	0.01451136	0.00691785	0.00457930	0.00286128	0–2 km	0.01431860	0.00679219	0.00448181	0.00277813	
	2–4 km	0.00847638	0.00404085	0.00267486	0.00167133	2–4 km	0.00826603	0.00390374	0.00256848	0.00158059	
2019-B6	4–6 km	0.00764725	0.00364559	0.00241322	0.00150785	4–6 km	0.00727824	0.00340505	0.00222659	0.00134867	66
	6–8 km	0.00804370	0.00383459	0.00253832	0.00158602	6–8 km	0.00742330	0.00343018	0.00222456	0.00131839	
	8–10 km	0.01237231	0.00589812	0.00390429	0.00243951	8–10 km	0.01188623	0.00558127	0.00365846	0.00222983	
	0–2 km	0.00882632	0.00374332	0.00292808	0.00181325	0–2 km	0.00834175	0.00342745	0.00268301	0.00160421	
	2–4 km	0.00515563	0.00218655	0.00171035	0.00105915	2–4 km	0.00462686	0.00184187	0.00144293	0.00083106	
2019-B7	4–6 km	0.00465132	0.00197267	0.00154305	0.00095555	4–6 km	0.00372370	0.00136800	0.00107391	0.00055540	50
	6–8 km	0.00489246	0.00207493	0.00162305	0.00100509	6–8 km	0.00333289	0.00105833	0.00083430	0.00033233	
	8–10 km	0.00752527	0.00319153	0.00249647	0.00154596	8–10 km	0.00630337	0.00239504	0.00187850	0.00101887	
	0–2 km	0.01723279	0.00879306	0.00576265	0.00383002	0–2 km	0.01667744	0.00843105	0.00548178	0.00359045	
	2–4 km	0.01006602	0.00513620	0.00336608	0.00223719	2–4 km	0.00946000	0.00474117	0.00305959	0.00197577	
2019-B8	4–6 km	0.00908140	0.00463380	0.00303682	0.00201835	4–6 km	0.00801827	0.00394079	0.00249914	0.00155975	58
	6–8 km	0.00955220	0.00487402	0.00319426	0.00212299	6–8 km	0.00776480	0.00370891	0.00229028	0.00135196	
	8–10 km	0.01469259	0.00749692	0.00491320	0.00326545	8–10 km	0.01329219	0.00658406	0.00420495	0.00266136	
	0–2 km	0.02375240	0.01420181	0.00926918	0.00626407	0–2 km	0.02328100	0.01389452	0.00903077	0.00606071	
	2–4 km	0.01387425	0.00829556	0.00541431	0.00365897	2–4 km	0.01335984	0.00796024	0.00515415	0.00343707	
2019-B9	4–6 km	0.01251713	0.00748412	0.00488471	0.00330106	4–6 km	0.01161470	0.00689587	0.00442831	0.00291178	55
	6–8 km	0.01316604	0.00787212	0.00513794	0.00347220	6–8 km	0.01164883	0.00688312	0.00437062	0.00281771	
	8–10 km	0.02025117	0.01210839	0.00790286	0.00534071	8–10 km	0.01906246	0.01133353	0.00730167	0.00482793	
	0–2 km	0.01723279	0.00879306	0.00576265	0.00383002	0–2 km	0.01698742	0.00863311	0.00563855	0.00372417	
	2–4 km	0.01006602	0.00513620	0.00336608	0.00223719	2–4 km	0.00979826	0.00496166	0.00323066	0.00212168	
2019-B10	4–6 km	0.00908140	0.00463380	0.00303682	0.00201835	4–6 km	0.00861167	0.00432760	0.00279925	0.00181573	47
	6–8 km	0.00955220	0.00487402	0.00319426	0.00212299	6–8 km	0.00876246	0.00435923	0.00279485	0.00178232	
	8–10 km	0.01469259	0.00749692	0.00491320	0.00326545	8–10 km	0.01407384	0.00709358	0.00460027	0.00299854	
	0–2 km	0.01451136	0.00691785	0.00457930	0.00286128	0–2 km	0.01395767	0.00655692	0.00429928	0.00262244	
	2–4 km	0.00847638	0.00404085	0.00267486	0.00167133	2–4 km	0.00787218	0.00364701	0.00236929	0.00141070	
2019-B11	4–6 km	0.00764725	0.00364559	0.00241322	0.00150785	4–6 km	0.00658731	0.00295467	0.00187715	0.00105062	63
	6–8 km	0.00804370	0.00383459	0.00253832	0.00158602	6–8 km	0.00626166	0.00267296	0.00163707	0.00081730	
	8–10 km	0.01237231	0.00589812	0.00390429	0.00243951	8–10 km	0.01097611	0.00498801	0.00319817	0.00183723	
	0–2 km	0.01933285	0.01161455	0.00865434	0.00607987	0–2 km	0.01911587	0.01147311	0.00854461	0.00598627	
	2–4 km	0.01129270	0.00678429	0.00505517	0.00355137	2–4 km	0.01105593	0.00662995	0.00493543	0.00344924	
2019-B12	4–6 km	0.01018809	0.00612068	0.00456070	0.00320399	4–6 km	0.00977272	0.00584991	0.00435062	0.00302481	54
	6–8 km	0.01071627	0.00643799	0.00479713	0.00337009	6–8 km	0.01001791	0.00598276	0.00444394	0.00306884	
	8–10 km	0.01648308	0.00990250	0.00737865	0.00518367	8–10 km	0.01593593	0.00954584	0.00710193	0.00494764	
	0–2 km	0.01723279	0.00879306	0.00576265	0.00383002	0–2 km	0.01637524	0.00823406	0.00532894	0.00346009	
	2–4 km	0.01006602	0.00513620	0.00336608	0.00223719	2–4 km	0.00913024	0.00452621	0.00289281	0.00183352	
2019-B13	4–6 km	0.00908140	0.00463380	0.00303682	0.00201835	4–6 km	0.00743976	0.00356369	0.00220657	0.00131020	48
	6–8 km	0.00955220	0.00487402	0.00319426	0.00212299	6–8 km	0.00679219	0.00307491	0.00179839	0.00093240	
	8–10 km	0.01469259	0.00749692	0.00491320	0.00326545	8–10 km	0.01253016	0.00608733	0.00381956	0.00233264	
	0–2 km	0.01451136	0.00691785	0.00457930	0.00286128	0–2 km	0.01419176	0.00670951	0.00441767	0.00272342	
	2–4 km	0.00847638	0.00404085	0.00267486	0.00167133	2–4 km	0.00812762	0.00381352	0.00249848	0.00152089	
2019-B14	4–6 km	0.00764725	0.00364559	0.00241322	0.00150785	4–6 km	0.00703543	0.00324678	0.00210379	0.00124393	63
	6–8 km	0.00804370	0.00383459	0.00253832	0.00158602	6–8 km	0.00701508	0.00316408	0.00201810	0.00114230	
	8–10 km	0.01237231	0.00589812	0.00390429	0.00243951	8–10 km	0.01156640	0.00537279	0.00349670	0.00209187	

Continued

	AOD	440 nm	675 nm	870 nm	1020 nm	AOD_{NO-BC}	440 nm	675 nm	870 nm	1020 nm	SZA /(°)
	0–2 km	0.01451136	0.00691785	0.00457930	0.00286128	0–2 km	0.01366388	0.00636541	0.00415069	0.00249570	
	2–4 km	0.00847638	0.00404085	0.00267486	0.00167133	2–4 km	0.00755159	0.00343803	0.00220716	0.00127241	
2019-B15	4–6 km	0.00764725	0.00364559	0.00241322	0.00150785	4–6 km	0.00602490	0.00258806	0.00159272	0.00080801	63
	6–8 km	0.00804370	0.00383459	0.00253832	0.00158602	6–8 km	0.00531612	0.00205661	0.00115886	0.00040941	
	8–10 km	0.01237231	0.00589812	0.00390429	0.00243951	8–10 km	0.01023529	0.00450510	0.00282350	0.00151766	
	0–2 km	0.01451136	0.00691785	0.00457930	0.00286128	0–2 km	0.01416164	0.00668988	0.00440243	0.00271042	
	2–4 km	0.00847638	0.00404085	0.00267486	0.00167133	2–4 km	0.00809475	0.00379209	0.00248186	0.00150671	
2019-B16	4–6 km	0.00764725	0.00364559	0.00241322	0.00150785	4–6 km	0.00697776	0.00320919	0.00207463	0.00121905	64
	6–8 km	0.00804370	0.00383459	0.00253832	0.00158602	6–8 km	0.00691812	0.00310088	0.00196907	0.00110048	
	8–10 km	0.01237231	0.00589812	0.00390429	0.00243951	8–10 km	0.01149044	0.00532327	0.00345828	0.00205910	
	0–2 km	0.01933285	0.01161455	0.00865434	0.00607987	0–2 km	0.01910161	0.01146382	0.00853740	0.00598012	
	2–4 km	0.01129270	0.00678429	0.00505517	0.00355137	2–4 km	0.01104037	0.00661981	0.00492756	0.00344253	
2019-B17	4–6 km	0.01018809	0.00612068	0.00456070	0.00320399	4–6 km	0.00974543	0.00583213	0.00433682	0.00301304	53
	6–8 km	0.01071627	0.00643799	0.00479713	0.00337009	6–8 km	0.00997204	0.00595286	0.00442074	0.00304906	
	8–10 km	0.01648308	0.00990250	0.00737865	0.00518367	8–10 km	0.01589999	0.00952241	0.00708375	0.00493214	
	0–2 km	0.02086156	0.01255429	0.00846475	0.00599573	0–2 km	0.02027290	0.01217057	0.00816703	0.00574180	
	2–4 km	0.01218565	0.00733321	0.00494443	0.00350223	2–4 km	0.01154330	0.00691449	0.00461956	0.00322513	
2019-B18	4–6 km	0.01099370	0.00661590	0.00446078	0.00315965	4–6 km	0.00986681	0.00588134	0.00389087	0.00267355	52
	6–8 km	0.01156364	0.00695889	0.00469204	0.00332346	6–8 km	0.00966906	0.00572390	0.00373386	0.00250619	
	8–10 km	0.01778645	0.01070372	0.00721700	0.00511193	8–10 km	0.01630208	0.00973613	0.00646628	0.00447161	
	0–2 km	0.01451136	0.00691785	0.00457930	0.00286128	0–2 km	0.01432244	0.00679470	0.00448376	0.00277979	
	2–4 km	0.00847638	0.00404085	0.00267486	0.00167133	2–4 km	0.00827022	0.00390647	0.00257060	0.00158240	
2019-B19	4–6 km	0.00764725	0.00364559	0.00241322	0.00150785	4–6 km	0.00728559	0.00340985	0.00223031	0.00135184	66
	6–8 km	0.00804370	0.00383459	0.00253832	0.00158602	6–8 km	0.00743567	0.00343824	0.00223081	0.00132373	
	8–10 km	0.01237231	0.00589812	0.00390429	0.00243951	8–10 km	0.01189592	0.00558759	0.00366336	0.00223402	
	0–2 km	0.01723279	0.00879306	0.00576265	0.00383002	0–2 km	0.01637965	0.00823694	0.00533117	0.00346199	
	2–4 km	0.01006602	0.00513620	0.00336608	0.00223719	2–4 km	0.00913506	0.00452935	0.00289525	0.00183560	
2019-B20	4–6 km	0.00908140	0.00463380	0.00303682	0.00201835	4–6 km	0.00744822	0.00356921	0.00221084	0.00131385	49
	6–8 km	0.00955220	0.00487402	0.00319426	0.00212299	6–8 km	0.00680640	0.00308417	0.00180558	0.00093853	
	8–10 km	0.01469259	0.00749692	0.00491320	0.00326545	8–10 km	0.01254130	0.00609459	0.00382519	0.00233744	
	0–2 km	0.01451136	0.00691785	0.00457930	0.00286128	0–2 km	0.01373791	0.00641367	0.00418813	0.00252764	
	2–4 km	0.00847638	0.00404085	0.00267486	0.00167133	2–4 km	0.00763238	0.00349069	0.00224801	0.00130725	
2019-B21	4–6 km	0.00764725	0.00364559	0.00241322	0.00150785	4–6 km	0.00616662	0.00268044	0.00166439	0.00086915	65
	6–8 km	0.00804370	0.00383459	0.00253832	0.00158602	6–8 km	0.00555438	0.00221192	0.00127936	0.00051220	
	8–10 km	0.01237231	0.00589812	0.00390429	0.00243951	8–10 km	0.01042197	0.00462678	0.00291791	0.00159819	
	0–2 km	0.01451136	0.00691785	0.00457930	0.00286128	0–2 km	0.01420468	0.00671794	0.00442420	0.00272899	
	2–4 km	0.00847638	0.00404085	0.00267486	0.00167133	2–4 km	0.00814172	0.00382271	0.00250561	0.00152697	
2019-B22	4–6 km	0.00764725	0.00364559	0.00241322	0.00150785	4–6 km	0.00706016	0.00326290	0.00211630	0.00125460	66
	6–8 km	0.00804370	0.00383459	0.00253832	0.00158602	6–8 km	0.00705666	0.00319118	0.00203913	0.00116024	
	8–10 km	0.01237231	0.00589812	0.00390429	0.00243951	8–10 km	0.01159898	0.00539402	0.00351318	0.00210592	
	0–2 km	0.01549402	0.00938374	0.00743462	0.00539028	0–2 km	0.01497801	0.00904737	0.00717365	0.00516768	
	2–4 km	0.00905037	0.00548123	0.00434271	0.00314857	2–4 km	0.00848729	0.00511418	0.00405793	0.00290567	
2019-B23	4–6 km	0.00816510	0.00494507	0.00391792	0.00284059	4–6 km	0.00717728	0.00430117	0.00341834	0.00241447	53
	6–8 km	0.00858839	0.00520144	0.00412104	0.00298785	6–8 km	0.00692762	0.00411886	0.00328111	0.00227144	
	8–10 km	0.01321012	0.00800052	0.00633872	0.00459572	8–10 km	0.01190893	0.00715234	0.00568064	0.00403442	

Continued

	AOD	440 nm	675 nm	870 nm	1020 nm	$AOD_{NO\text{-}BC}$	440 nm	675 nm	870 nm	1020 nm	SZA /(°)
	0–2 km	0.00882632	0.00374332	0.00292808	0.00181325	0–2 km	0.00760645	0.00294815	0.00231114	0.00128703	
	2–4 km	0.00515563	0.00218655	0.00171035	0.00105915	2–4 km	0.00382450	0.00131885	0.00103714	0.00048494	
2019-B24	4–6 km	0.00465132	0.00197267	0.00154305	0.00095555	4–6 km	0.00231612	0.00045046	0.00036203	0	56
	6–8 km	0.00489246	0.00207493	0.00162305	0.00100509	6–8 km	0.00096639	0	0	0	
	8–10 km	0.00752527	0.00319153	0.00249647	0.00154596	8–10 km	0.00444925	0.00118642	0.00094078	0.00021905	
	0–2 km	0.00932006	0.00435418	0.00329534	0.00183911	0–2 km	0.00906990	0.00419111	0.00316882	0.00173120	
	2–4 km	0.00544403	0.00254336	0.00192487	0.00107426	2–4 km	0.00517105	0.00236542	0.00178681	0.00095651	
2019-B25	4–6 km	0.00491152	0.00229458	0.00173659	0.00096918	4–6 km	0.00443263	0.00198241	0.00149439	0.00076260	48
	6–8 km	0.00516614	0.00241354	0.00182662	0.00101943	6–8 km	0.00436100	0.00188870	0.00141942	0.00067211	
	8–10 km	0.00794624	0.00371235	0.00280959	0.00156802	8–10 km	0.00731542	0.00330115	0.00249055	0.00129590	
	0–2 km	0.01063189	0.00485133	0.00353127	0.00223195	0–2 km	0.01023935	0.00459546	0.00333274	0.00206262	
	2–4 km	0.00621030	0.00283376	0.00206268	0.00130373	2–4 km	0.00578195	0.00255454	0.00184605	0.00111895	
2019-B26	4–6 km	0.00560283	0.00255657	0.00186092	0.00117620	4–6 km	0.00485138	0.00206674	0.00148088	0.00085205	49
	6–8 km	0.00589329	0.00268911	0.00195739	0.00123718	6–8 km	0.00462992	0.00186558	0.00131845	0.00069219	
	8–10 km	0.00906469	0.00413622	0.00301074	0.00190295	8–10 km	0.00807486	0.00349100	0.00251013	0.00147596	
	0–2 km	0.04008696	0.02400511	0.01579334	0.01074900	0–2 km	0.03994293	0.02391122	0.01572050	0.01068687	
	2–4 km	0.02341559	0.01402186	0.00922520	0.00627870	2–4 km	0.02325842	0.01391941	0.00914572	0.00621090	
2019-B27	4–6 km	0.02112517	0.01265029	0.00832283	0.00566455	4–6 km	0.02084944	0.01247056	0.00818338	0.00554560	47
	6–8 km	0.02222035	0.01330612	0.00875431	0.00595821	6–8 km	0.02175678	0.01300394	0.00851986	0.00575824	
	8–10 km	0.03417793	0.02046662	0.01346532	0.00916454	8–10 km	0.03381473	0.02022987	0.01328163	0.00900787	
	0–2 km	0.00882632	0.00374332	0.00292808	0.00181325	0–2 km	0.00799931	0.00320423	0.00250983	0.00145650	
	2–4 km	0.00515563	0.00218655	0.00171035	0.00105915	2–4 km	0.00425319	0.00159829	0.00125395	0.00066987	
2019-B28	4–6 km	0.00465132	0.00197267	0.00154305	0.00095555	4–6 km	0.00306817	0.00094069	0.00074238	0.00027262	56
	6–8 km	0.00489246	0.00207493	0.00162305	0.00100509	6–8 km	0.00223078	0.00033991	0.00027691	0	
	8–10 km	0.00752527	0.00319153	0.00249647	0.00154596	8–10 km	0.00543988	0.00183217	0.00144179	0.00064638	
	0–2 km	0.01933285	0.01161455	0.00865434	0.00607987	0–2 km	0.01907730	0.01144797	0.00852510	0.00596964	
	2–4 km	0.01129270	0.00678429	0.00505517	0.00355137	2–4 km	0.01101385	0.00660252	0.00491415	0.00343108	
2019-B29	4–6 km	0.01018809	0.00612068	0.00456070	0.00320399	4–6 km	0.00969890	0.00580179	0.00431329	0.00299297	49
	6–8 km	0.01071627	0.00643799	0.00479713	0.00337009	6–8 km	0.00989381	0.00590186	0.00438118	0.00301531	
	8–10 km	0.01648308	0.00990250	0.00737865	0.00518367	8–10 km	0.01583870	0.00948246	0.00705275	0.00490570	
	0–2 km	0.01907020	0.01106026	0.00773422	0.00516714	0–2 km	0.01845137	0.01065687	0.00742125	0.00490019	
	2–4 km	0.01113928	0.00646052	0.00451771	0.00301823	2–4 km	0.01046401	0.00602034	0.00417619	0.00272693	
2019-B30	4–6 km	0.01004968	0.00582857	0.00407581	0.00272300	4–6 km	0.00886505	0.00505637	0.00347668	0.00221198	52
	6–8 km	0.01057068	0.00613074	0.00428711	0.00286416	6–8 km	0.00857901	0.00483246	0.00327982	0.00200501	
	8–10 km	0.01625915	0.00942992	0.00659415	0.00440547	8–10 km	0.01469871	0.00841274	0.00580496	0.00373234	
	0–2 km	0.02086156	0.01255429	0.00846475	0.00599573	0–2 km	0.02041995	0.01226642	0.00824141	0.00580523	
	2–4 km	0.01218565	0.00733321	0.00494443	0.00350223	2–4 km	0.01170376	0.00701909	0.00470071	0.00329435	
2019-B31	4–6 km	0.01099370	0.00661590	0.00446078	0.00315965	4–6 km	0.01014832	0.00606484	0.00403323	0.00279498	51
	6–8 km	0.01156364	0.00695889	0.00469204	0.00332346	6–8 km	0.01014233	0.00603241	0.00397322	0.00271035	
	8–10 km	0.01778645	0.01070372	0.00721700	0.00511193	8–10 km	0.01667288	0.00997784	0.00665381	0.00463157	
	0–2 km	0.00882632	0.00374332	0.00292808	0.00181325	0–2 km	0.00846475	0.00350763	0.00274522	0.00165727	
	2–4 km	0.00515563	0.00218655	0.00171035	0.00105915	2–4 km	0.00476108	0.00192936	0.00151081	0.00088896	
2019-B32	4–6 km	0.00465132	0.00197267	0.00154305	0.00095555	4–6 km	0.00395917	0.00152148	0.00119300	0.00065697	51
	6–8 km	0.00489246	0.00207493	0.00162305	0.00100509	6–8 km	0.00372877	0.00131638	0.00103451	0.00050311	
	8–10 km	0.00752527	0.00319153	0.00249647	0.00154596	8–10 km	0.00661354	0.00259722	0.00203536	0.00115267	

Continued

	AOD	440 nm	675 nm	870 nm	1020 nm	$AOD_{NO\text{-}BC}$	440 nm	675 nm	870 nm	1020 nm	SZA /(°)
	0–2 km	0.02086156	0.01255429	0.00846475	0.00599573	0–2 km	0.02052142	0.01233257	0.00829272	0.00584901	
	2–4 km	0.01218565	0.00733321	0.00494443	0.00350223	2–4 km	0.01181449	0.00709127	0.00475671	0.00334212	
2019-B33	4–6 km	0.01099370	0.00661590	0.00446078	0.00315965	4–6 km	0.01034257	0.00619146	0.00413147	0.00287877	83
	6–8 km	0.01156364	0.00695889	0.00469204	0.00332346	6–8 km	0.01046892	0.00624529	0.00413839	0.00285122	
	8–10 km	0.01778645	0.01070372	0.00721700	0.00511193	8–10 km	0.01692876	0.01014463	0.00678322	0.00474194	
	0–2 km	0.02086156	0.01255429	0.00846475	0.00599573	0–2 km	0.02059594	0.01238114	0.00833041	0.00588115	
	2–4 km	0.01218565	0.00733321	0.00494443	0.00350223	2–4 km	0.01189580	0.00714427	0.00479784	0.00337719	
2019-B34	4–6 km	0.01099370	0.00661590	0.00446078	0.00315965	4–6 km	0.01048522	0.00628445	0.00420362	0.00294031	79
	6–8 km	0.01156364	0.00695889	0.00469204	0.00332346	6–8 km	0.01070875	0.00640163	0.00425968	0.00295468	
	8–10 km	0.01778645	0.01070372	0.00721700	0.00511193	8–10 km	0.01711666	0.01026711	0.00687825	0.00482300	
	0–2 km	0.02086156	0.01255429	0.00846475	0.00599573	0–2 km	0.02071000	0.01245549	0.00838810	0.00593035	
	2–4 km	0.01218565	0.00733321	0.00494443	0.00350223	2–4 km	0.01202026	0.00722540	0.00486078	0.00343088	
2019-B35	4–6 km	0.01099370	0.00661590	0.00446078	0.00315965	4–6 km	0.01070356	0.00642677	0.00431405	0.00303449	82
	6–8 km	0.01156364	0.00695889	0.00469204	0.00332346	6–8 km	0.01107584	0.00664091	0.00444534	0.00311303	
	8–10 km	0.01778645	0.01070372	0.00721700	0.00511193	8–10 km	0.01740427	0.01045459	0.00702371	0.00494707	
	0–2 km	0.02086156	0.01255429	0.00846475	0.00599573	0–2 km	0.02064074	0.01241035	0.00835307	0.00590048	
	2–4 km	0.01218565	0.00733321	0.00494443	0.00350223	2–4 km	0.01194469	0.00717614	0.00482256	0.00339828	
2019-B36	4–6 km	0.01099370	0.00661590	0.00446078	0.00315965	4–6 km	0.01057098	0.00634035	0.00424700	0.00297730	83
	6–8 km	0.01156364	0.00695889	0.00469204	0.00332346	6–8 km	0.01085294	0.00649562	0.00433261	0.00301688	
	8–10 km	0.01778645	0.01070372	0.00721700	0.00511193	8–10 km	0.01722964	0.01034075	0.00693539	0.00487173	
	0–2 km	0.02227230	0.01267453	0.00869016	0.00584366	0–2 km	0.02184645	0.01239693	0.00847478	0.00565996	
	2–4 km	0.01300970	0.00740344	0.00507610	0.00341340	2–4 km	0.01254499	0.00710053	0.00484107	0.00321294	
2019-B37	4–6 km	0.01173714	0.00667927	0.00457957	0.00307951	4–6 km	0.01092191	0.00614786	0.00416727	0.00272785	49
	6–8 km	0.01234562	0.00702553	0.00481699	0.00323916	6–8 km	0.01097501	0.00613210	0.00412381	0.00264792	
	8–10 km	0.01898925	0.01080623	0.00740918	0.00498227	8–10 km	0.01791540	0.01010624	0.00686609	0.00451904	
	0–2 km	0.09615487	0.05989906	0.03789197	0.02636781	0–2 km	0.09585808	0.05970560	0.03774186	0.02623978	
	2–4 km	0.05616597	0.03498823	0.02213345	0.01540196	2–4 km	0.05584211	0.03477712	0.02196966	0.01526226	
2019-B38	4–6 km	0.05067203	0.03156582	0.01996844	0.01389540	4–6 km	0.05010388	0.03119547	0.01968110	0.01365032	44
	6–8 km	0.05329899	0.03320227	0.02100365	0.01461577	6–8 km	0.05234378	0.03257961	0.02052056	0.01420372	
	8–10 km	0.08198113	0.05106962	0.03230649	0.02248105	8–10 km	0.08123274	0.05058178	0.03192799	0.02215822	
	0–2 km	0.09615487	0.05989906	0.03789197	0.02636781	0–2 km	0.09586155	0.05970786	0.03774362	0.02624128	
	2–4 km	0.05616597	0.03498823	0.02213345	0.01540196	2–4 km	0.05584590	0.03477959	0.02197157	0.01526389	
2019-B39	4–6 km	0.05067203	0.03156582	0.01996844	0.01389540	4–6 km	0.05011052	0.03119980	0.01968446	0.01365318	57
	6–8 km	0.05329899	0.03320227	0.02100365	0.01461577	6–8 km	0.05235494	0.03258689	0.02052620	0.01420854	
	8–10 km	0.08198113	0.05106962	0.03230649	0.02248105	8–10 km	0.08124148	0.05058748	0.03193241	0.02216199	

Note: $AOD_{NO\text{-}BC}$ represents the aerosol optical depth in the absence of BC.

Text S1 SBDART model parameters

The following equations (1), (2) and (3) were used to computes the wavelength-dependent aerosol absorption coefficient of BC (b_{BC}), the particle single scattering albedo (a_{SSA}) and aerosol optical depth (d_{AOD}) for each altitude layer.

$$b_{BC}(\lambda) = M_{BC} \times x(660) \times (\frac{\lambda}{660})^{-y} \tag{1}$$

$$a_{SSA}(\lambda) = \frac{b_{scat}(\lambda)}{b_{scat}(\lambda) + b_{BC}(\lambda)} \tag{2}$$

$$d_{AOD} = \sum_{i=1}^{n} \mathrm{Ext}(\lambda)\tau_i = \sum_{i=1}^{n} (b_{scat}(\lambda) + b_{BC}(\lambda))\tau_i \tag{3}$$

where M_{BC} is the mass concentration of BC, x is the mass absorption cross-section for BC and y is the absorption Ångström exponent for BC. The value of x (10 $m^2 \cdot g^{-1}$) and y used in our calculation in agreement with the atmospheric relevant range suggested by previous studies (Chung et al., 2012; Olson et al., 2015). Ext is the extinction coefficient averaged in the i-th altitude bin with a thickness of τ_i. Vertically resolved data were binned every 2 km. The direct radiative effect was calculated under a clear sky condition and a mean solar zenith angle computed from the specified date and geographic coordinates using an internal solar ephemeris algorithm.

Text S2 BC calculation

Based on the ratio of Lev to total and organic carbon $R_{TC/Lev,\ bb}$ and $R_{OC/Lev,\ bb}$ released by biomass burning observed in previous studies and the Lev concentration measured in this study, we calculated (1) TC from biomass burning $C_{TC,\ bb} = C_{Lev} \times R_{TC/Lev,\ bb}$ and (2) OC from biomass burning $C_{OC,\ bb} = C_{Lev} \times R_{OC/Lev,\ bb}$. The elemental carbon concentration (EC_{bb}) of biomass burning was estimated by subtracting (2) from (1) (Saarikoski et al., 2007; Yttri et al., 2014).

In this study, we used EC for BC. In some climate models and health studies, EC concentrations are often as a surrogate of BC concentrations when BC measurements are not possible (Peng et al., 2016; Zhang et al., 2017). However, previous studies investigated the difference between BC and EC concentrations from different measurements, and attributed to the differences to the light absorptivity of BC (Jeong et al., 2004; Liu et al., 2022; Salako et al., 2012; Park et al., 2002). Such as, Park et al. (2002) found the relationship between EC and BC measurements in $PM_{2.5}$ reflected very good agreement and BC/EC slopes about 1. Salako et al. (2012) showed the variation between BC and EC at Asia and Pacific regions. Jeong et al. (2004) found BC was higher than EC in the cases of higher sulfate concentration, while BC was lower than EC in forest fire events. Liu et al. (2022) showed that around 90% of BC concentration was higher than that of EC in three-year continuous measurement in Beijing, China. The relationship between BC and EC concentration remains uncertain, while, the concentration of BC is an important parameter for calculating the optical thickness of black carbon aerosol, hence, in this paper, when EC is used to calculate the radiative forcing of BC, only an approximate radiative forcing value can be obtained.

References

Chung C E, Ramanathan V, Decremer D. 2012. Observationally constrained estimates of carbonaceous aerosol radiative forcing. Proc Natl Acad Sci USA, 109(29): 11624-11629, doi:10.1073/pnas.1203707109.

Jeong C H, Hopke P K, Kim E, et al. 2004. The comparison between thermal-optical transmittance elemental carbon and Aethalometer black carbon measured at multiple monitoring sites. Atmos Environ, 38(31): 5193-5204, doi:10.1016/j.atmosenv.2004.02.065.

Liu X, Zheng M, Liu Y, et al. 2022. Intercomparison of equivalent black carbon (eBC) and elemental carbon (EC) concentrations with three-year continuous measurement in Beijing, China. Environ Res, 209: 112791, doi:10.1016/j.envres.2022.112791.

Olson M R, Victoria Garcia M, Robinson M A, et al. 2015. Investigation of black and brown carbon multiple-wavelength-dependent light absorption from biomass and fossil fuel combustion source emissions. J Geophys Res Atmos, 120(13): 6682-6697, doi:10.1002/2014jd022970.

Park S S, Kim Y J, Fung K. 2002. $PM_{2.5}$ carbon measurements in two urban areas: Seoul and Kwangju, Korea. Atmos Environ, 36(8): 1287-1297, doi:10.1016/S1352-2310(01)00552-0.

Peng J, Hu M, Guo S, et al. 2016. Markedly enhanced absorption and direct radiative forcing of black carbon under polluted urban environments. Proc Natl Acad Sci USA, 113(16): 4266-4271, doi:10.1073/pnas.1602310113.

Saarikoski S, Sillanpää M, Sofiev M, et al. 2007. Chemical composition of aerosols during a major biomass burning episode over northern Europe in spring 2006: experimental and modelling assessments. Atmos Environ, 41(17): 3577-3589, doi:10.1016/j.atmosenv.2006.12.053.

Salako G O, Hopke P K, Cohen D D, et al. 2012. Exploring the variation between EC and BC in a variety of locations. Aerosol Air Qual Res, 12(1): 1-7, doi:10.4209/aaqr.2011.09.0150.

Yttri K E, Lund Myhre C, Eckhardt S, et al. 2014. Quantifying black carbon from biomass burning by means of levoglucosan–a one-year time series at the Arctic Observatory Zeppelin. Atmos Chem Phys, 14(12): 6427-6442, doi:10.5194/acp-14-6427-2014.

Zhang Y, Kang S, Cong Z, et al. 2017. Light-absorbing impurities enhance glacier albedo reduction in the southeastern Tibetan Plateau. J Geophys Res Atmos, 122(13): 6915-6933, doi:10.1002/2016jd026397.